Image phase shift invariance based cloud motion displacement vector calculation method for ultra-short-term solar PV power forecasting

Fei Wang [1, 2, *], Zhao Zhen [1], Chun Liu [3], Zengqiang Mi [1], Bri-Mathias Hodge [4], Miadreza Shafie-khah [5], João P.S. Catalão [5, 6, 7]

1. State Key Laboratory of Alternate Electrical Power System With Renewable Energy Sources (North China Electric Power University), Baoding 071003, China
2. Department of Electrical and Computer Engineering, University of Illinois at Urbana-Champaign, Urbana, IL 61801, USA
3. State Key Laboratory of Operation and Control of Renewable Energy & Storage Systems, China Electric Power Research Institute, Beijing 100192, China
4. National Renewable Energy Laboratory, Golden, CO 80401 USA
5. C-MAST, University of Beira Interior, Covilhã 6201-001, Portugal
6. INESC TEC and the Faculty of Engineering of the University of Porto, Porto 4200-465, Portugal
7. INESC-ID, Instituto Superior Técnico, University of Lisbon, Lisbon 1049-001, Portugal

Abstract: Irradiance received on the earth's surface is the main factor affecting the output power of solar PV plants, and chiefly determined by the cloud distribution seen in a ground-based sky image at the corresponding moment in time. Obtaining the cloud distribution in future sky images from the accurate calculation of cloud motion displacement vectors (CMDVs) using historical sky images is the foundation for those linear extrapolation-based ultra-short-term solar PV power forecasting approaches. Theoretically, the CMDV can be obtained from the coordinate of the peak pulse calculated using a Fourier phase correlation theory (FPCT) method through the frequency domain information of sky images. The peak pulse is significant and unique only when the cloud deformation between two consecutive sky images is slight enough, which is likely possible for a very short time interval (such as 1 min or shorter) and common changes in the speed of clouds. Sometimes, there will appear more than one pulse with similar values when the deformation of the clouds between two consecutive sky images is comparatively obvious under fast changing cloud speeds. This would probably lead to significant errors if the CMDVs were still only obtained from the single coordinate of the peak value pulse. However, the deformation estimation of clouds between two images and its influence on FPCT-based CMDV calculations are terrifically complex and difficult because the motion of clouds is complicated to describe and model. Therefore, to improve the accuracy and reliability under these circumstances in a simple manner, an image-phase-shift-invariance (IPSI) based CMDV calculation method using FPCT is proposed for minute time scale solar power forecasting. First, multiple different CMDVs are calculated using the FPCT method from consecutive images according to different rotation angles, compared to the original images. Second, the final CMDV is generated from all of the calculated CMDVs through a centroid iteration strategy based on its density and distance distribution. Third, the influence of different rotation angle resolution on the final CMDV is analyzed as a means of parameter estimation. Simulations under various scenarios, including both various cloud cover conditions indicated that the proposed IPSI-based CMDV calculation method using FPCT is more accurate and reliable than the original FPCT method, optimal flow (OF) method, and particle image velocimetry (PIV) method.

Keywords: phase correlation; Fourier transform; cloud motion displacement vector; sky image; solar forecasting

---

1 Introduction

1.1 Background and literature review

In recent years, global renewable energy has grown rapidly against the background of increasing global energy consumption, especially in developing countries. In 2015 renewables accounted for an estimated more than 60% of net additions to global power generating capacity [1], among which the solar photovoltaics (PV), wind, and hydropower contributed the majority of installations. By the end of 2015, renewables produced an estimated 27.7% of the world's power-generating capacity and are sufficient to supply about 22.8% of global electricity demand [2]. However, the rapid development of solar power generation also brings a number of challenges.

Nomenclature

Acronyms		*Symbols*	
CMDV	Cloud motion displacement vector	$f(x,y)$	The grayscale matrix of sky image
FPCT	Fourier phase correlation theory	$F(u,v)$	The 2-D Discrete Fourier transform of sky image grayscale matrix
IPSI	Image-phase-shift-invariance	$\Delta\emptyset(u,v)$	The phase difference spectrum
PIV	Particle image velocimetry	$C(u,v)$	The cross-power spectrum
UST-SPPF	Ultra-short-term solar PV power forecasting	$f_R(x,y)$	The displacement response matrix
DFT	Discrete Fourier transform	$\delta(x-x_0,y-y_0)$	The pulse matrix
CPS	Cross-power spectrum	θ	Rotation angle degree
DRM	Displacement response matrix		

The nonlinear, stochastic nature of solar radiation translates directly into the power generated by solar PV installations. The resulting fluctuations in power output from grid-connected PV system lead to the potential of reducing grid reliability and the difficulties in the control of load-generation balancing. The optimal operation of power systems with high penetrations of solar PV has become an important challenge which need to be addressed through a number of means, including unit commitment, economic dispatch and scenarios with flexible loads like demand response [3–6].

As the key factor impacting the output power of solar PV plants, solar irradiance forecasting is an important technology for reducing the uncertainty in PV power generations [7–10]. Especially in cloudy weather conditions, the solar irradiance on the ground can fluctuant significantly at the minute level, which brings a great many difficulties for solar irradiance forecasting in intra-hour [11,12] instead of hourly [13] or daily [14] time scales. One approach for producing better forecasts is to observe the local cloud distributions through direct observation of the sky above the solar PV station with high spatial and temporal resolution [15,16]. For most ultra-short-term solar PV power forecasting (UST-SPPF) approaches at minute time scale, sky images are important data sources to provide clouds locations at different times. In previous studies, different kinds of digital image processing techniques were utilized to track cloud motion and calculate the displacement of clouds in sky images [17,18]. Then the cloud distribution in a future sky image is predicted based on linear extrapolation. Subsequently, the ground solar irradiance can be calculated according to the predicted cloud distribution in sky images and converted to solar PV output power [19,20].

The current techniques using digital image process for cloud tracking and displacement calculation can be divided into two categories: the gray scale information based methods and the Fourier translation based methods. The former methods calculate the object displacement in image according to the correlation or similarity of gray scale distribution. The latter method is based on the principle that the frequency spectrum of the image in the Fourier domain will also change correspondingly when the clouds in a sky image moved. The detail introduction and literature review on the above two categories methods are as follows.

Generally, there are four popular gray scale information based methods to derivate cloud velocity: scale invariant feature transform (SIFT), optical flow (OF), X-correlation (X-corr), and particle image velocimetry (PIV). The SIFT method extracts key points of cloud image according to scale invariant feature transform and then tracks these key points to derivate cloud velocity [21,22]. In the tracking process proposed by [23], merging and splitting of clouds are handled via checking matched pairs of feature points among different clusters. Afterwards, the tracking information of feature points is utilized to predict if the sun will be covered or obscured by clouds within the prediction horizon. The OF method calculates cloud pixel displacement based on the assumption that the gray scale value of an image pixel remains constant during the cloud motion [24,25], which is recently introduced in the research of solar forecasts for cloud velocity derivation [26,27]. In [28], a variational optical flow (VOF) technique was utilized to determine the sub-pixel accuracy of cloud motion for every pixel, then cloud locations up to 15min ahead can be forecasted by inverse mapping of the cloud map. The X-corr and PIV method all calculate the cloud velocity based on the matching correlation between two images, but the former focuses on the whole image while the latter one needs to segment the image first [29]. In [11,15,30], PIV method is applied to calculate the cloud velocity based on image segmentation and matching, then the future position of cloud is obtained by linear extrapolation. The above methods are analyzed and quantitatively evaluated in recent research [31], which indicated that PIV method shows higher accuracy than the other methods in CMDV calculation. However, the performance of PIV method is usually inconsistent when dealing with sky images in which the brightness and shape of cloud changing rapidly [32].

Unlike the gray scale information based methods, Fourier translation based methods use unified technical proposal of Fourier phase correlation theory (FPCT) and it can describe the image discrepancy more thoroughly mathematical [33].

The changes of some abstract features, such as object contour, will reflect in the frequency domain and can be analyzed through calculation. In practical application, Fourier translation based methods also require less computation and thus less processing time[34]. For example, the displacement of clouds in sky images is calculated based on the analysis of the phase shifting between the spectrums of two consecutive images in early researches such as [35–37]. Despite these advantages, the Fourier translation based methods require us to analyze and compute images in the frequency domain. Therefore, the influence of cloud deformation and interferences from the sun and sky background in actual sky images will be different with it appeared in time domain when using Fourier translation based methods to estimate cloud displacement [28,38].

1.2 Motivation and contribution

The differences in algorithm principle of the gray scale information based methods and the Fourier translation based methods lead to different performance characteristics. For example, PIV method calculates image displacement according to the similarity of object shape and color in the images, while cloud deformation and other interferences will affect the similarity index value. Fourier translation based FPCT method focus on the global characteristics of the images, through which not only the image displacement is transformed into phase shift in frequency domain, but also the cloud deformation and other interferences are also transformed into random noise signals in frequency domain. Therefore, in the cases with cloud deformation and other image interferences, the PIV method is more reliable than FPCT method since it can always provide an available result although it may be not that accurate, while the results of FPCT method exhibit lower reliability because its results could be either very precise or entirely inaccurate, so as to be totally unusable at all.

However, it is a very complicated task to describe and model cloud motion in a mathematical way using sky images, even with the assistance of artificial perception and judgment. Moreover, the FPCT method transforming image data into frequency domain further increase the difficulties in analyzing the influences of cloud displacement and deformation on the performance, which restricts the application of FPCT method in the recent literature about sky image based solar power forecasting.

Therefore, to overcome the disadvantage of insufficient reliability of FPCT method and provide a both accurate and reliable CMDV calculation approach, an image-phase-shift-invariance (IPSI) based CMDV calculation method using FPCT for minute time scale solar irradiance forecasting is proposed. For two consecutive images, phase shift between these two images is invariant before and after the synchronous rotation for these two images in any angle. A certain number (depends on the specific rotation angle interval) of consecutive image pairs with the same theoretical phase shift can be obtained through the synchronous image rotation. Then multiple CMDVs are calculated using FPCT method. To generate the final CMDV result, these CMDVs are further refined through a proposed centroid iteration algorithm. The proposed IPSI based CMDV calculation can eliminate random errors of FPCT method to improve its reliability so as to achieve a much higher average accuracy than the original FPCT method.

The main contributions of this paper include:

(1) Expanding the IPSI in terms of the synchronous rotation of two images, which can effectively reflect the invariable cross correlation characteristic on the image displacement of two consecutive images in frequency domain.

(2) An IPSI-based CMDV calculation method using FPCT is proposed, which generates the final CMDV result through a statistical process algorithm named centroid iteration using multiple CMDVs obtained by the synchronous rotation of historical sky images.

(3) The comparison between the IPSI-based method, original FPCT method, and two current well-established methods (PIV and OF) is simulated to verify the effectiveness and evaluate the performance of the proposed method.

The rest of this paper is organized as follows. Section 2 introduces the cloud motion influence on PV power generation and the sky image based minute time scale UST-SPPF method. Section 3 introduces the mathematical foundation of FPCT. Then section 4 proposes an IPSI based CMDV calculation method using FPCT. Section 5 presents the results and discussion, in which the algorithm performances of the proposed IPSI-based method, original FPCT-method, PIV method, and OF method are compared. Finally, conclusions are drawn in Section 6.

2 Sky image based ultra-short-term solar PV power forecasting

2.1 Influence of cloud motion on PV power generation

Surface solar irradiance is the main determining factor of PV power output. The combined effects of sun and cloud motion determine their relative position and influence the surface solar irradiance directly. At the time scale of intra-hour or even the minute level, the motion of the sun is almost negligible. Then the motion of clouds becomes the key element to affect the irradiance value. Thus, it is the generation, dissipation, and movement of clouds that mainly cause changes at these time scales, and further leads to rapid fluctuations in surface irradiance and PV power output.

In sky images recorded at different times, the differences of cloud distribution around a PV power station can be classified into two categories: (1) the shape and position of the cloud are different, or (2) the shape is basically the same but the position of the cloud is different. Which category the cloud distribution belongs to depends on the time interval between sky images and the atmospheric environment. Longer time intervals and more variable atmospheric conditions, lead to a higher probability of the former condition.

However, the generation, dissipation, and deformation of clouds are complex atmospheric physics processes. Influenced by inertia, the changes in cloud shape need a certain amount of time to accumulate and then be reflected in the sky images. Usually, for two sky images with a time interval of about 1 minute or even shorter, the atmospheric changes are not yet able to impact the shape of clouds significantly, except for a few unusual severe weather conditions. This time interval can be longer in the case of a stable atmospheric environment. In the above cases, we can consider that the shape of the clouds remains the same, only the locations are different. A large number of actually measured sky images in different regions in China have shown this empirically. Therefore, for sky image based UST-SPPF approaches, it is theoretically feasible for the CMDV calculation based on historical image sequences and then predicting the cloud distribution in a future sky image using linear extrapolation.

2.2 Sky image based PV power forecasting approach

The traditional process of sky image based UST-SPPF is shown in Figure 1. This kind of PV power forecasting method focuses on the sky image sequences obtained by ground-based observation at the PV power station. First, under the premise of consistent cloud shape and velocity, the displacement of clouds at a given time interval can be calculated. Then the cloud distribution can be predicted using linear extrapolation. Finally, as the position of the sun in the sky image can be calculated according to the date, time, latitude, and longitude of the observation equipment, the PV power output is then calculated according to the 'clouds-irradiance–power' mapping model to realize the power forecast [11,15,20].

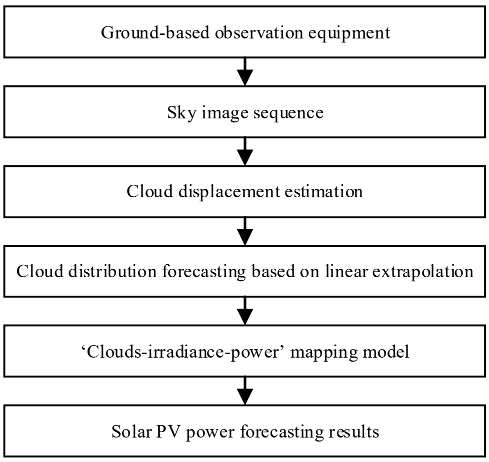

Figure 1. Sky image based UST-SPPF process.

The sky image based UST-SPPF process includes multiple relatively independent sub-processes. These sub-processes are logically ordered and need to be studied individually. Among them, the calculation of CMDV is a key sub-process. It is the foundation for the following ground irradiance forecasting and can greatly affect the accuracy of the final PV power forecasting results. Therefore, to lay the foundation for UST-SPPF, it is necessary to study on the algorithms for CMDV calculation and improve their accuracy.

Usually, the cloud height does not change as dramatically as its horizontal position and can be regarded as a fixed value. However, the height of the cloud base is also an important parameter for perspective rectification in sky images, which is a very necessary process before CMDV calculation. Due to the lack of effective means of observation, precise vertical information of cloud heights is often unavailable. Therefore, a general estimate of cloud base height considering image distortion is applied and we mainly focus on the horizontal position of clouds in the sky images in this research.

2.3 Ground-based sky image observation equipment

Figure 2. EKO sky camera.

The automatic sky imaging system used in this work as shown in Figure 2 consists of a sky camera and its supporting software produced by EKO INSTRUMENTS acquires the sky images used in this paper. The sky camera is installed at the Yunnan Electric Power Research Institute in Yunnan province of China (geographical coordinates: E102°47′, N24° 59′). The viewing angle of the camera is 120° and the time interval between two consecutive sky images is one minute. The supporting software of the sky camera is used for basic image preprocessing, including the perspective rectification, identification of cloud type based on cloud thickness, and sun position calculation. In this paper, perspective rectification has been performed on all images by the supporting software.

3 CMDV calculation using FPCT

3.1 Fourier phase correlation theory

The Fourier transform algorithm is a commonly used image transforming method. The Fast Fourier Transform (FFT) technique enabled us to process the information of a high-resolution image in the frequency domain in a very short time [39–41]. Let $f(x,y)$ be the grayscale matrix of an $M \times N$ image, the 2-D Discrete Fourier transform (DFT) of the grayscale matrix is:

$$F(u,v)=\sum_{x=0}^{M-1}\sum_{y=0}^{N-1} f(x,y)\mathrm{e}^{-j2\pi(\frac{ux}{M}+\frac{vy}{N})}=|F(u,v)|\mathrm{e}^{-j\phi(u,v)} \quad (u=0,1,\ldots,M-1,\quad v=0,1,\ldots,N-1) \tag{1}$$

where x, y are coordinate variables in the original image and u, v are coordinate variables in the Fourier transform of th original image. Respectively, $|F(u,v)|$ is the amplitude spectrum of the image, which characterizes the frequency of each grayscale value, and $\emptyset(u,v)$ is the phase spectrum, which characterizes the spatial structure of the image [42].

If $f_1(x,y)$ and $f_2(x,y)$ are grayscale matrixes of two images that differ only by a displacement (x_0,y_0), $F_1(u,v)$ and $F_2(u,v)$ are their Fourier transforms, then:

$$f_2(x,y)=f_1(x-x_0,y-y_0) \tag{2}$$

According to the Fourier translation property:

$$F_2(u,v)=F_1(u,v)\mathrm{e}^{-\mathrm{j}2\pi(\frac{ux_0}{M}+\frac{vy_0}{N})} \tag{3}$$

According to function (1), function (3) can be rewritten as

$$|F_2(u,v)|\mathrm{e}^{-\mathrm{j}\phi_2(u,v)} = |F_1(u,v)|\mathrm{e}^{-\mathrm{j}[\phi_1(u,v)+2\pi(\frac{ux_0}{M}+\frac{vy_0}{N})]} \tag{4}$$

For the two images that only differ by a displacement, their amplitude spectrums would be the same, i.e. $|F_1(u,v)| = |F_2(u,v)|$. Then the difference in phase spectrum is calculated as

$$\Delta\phi(u,v) = \phi_1(u,v) - \phi_2(u,v) = -2\pi(\frac{ux_0}{M}+\frac{vy_0}{N}) \tag{5}$$

It will be a two-dimensional periodic signal with cycle times of M/x_0 in u-axis and N/y_0 in v-axis after the modular arithmetic of $\Delta\emptyset(u,v)$ by 2π. This means the displacement of images will be represented as the phase shift in the frequency domain.

The cross-power spectrum (CPS) of $F_1(u,v)$ and $F_2(u,v)$ is defined as:

$$C(u,v) = \frac{F_1(u,v)F_2^*(u,v)}{|F_1(u,v)F_2^*(u,v)|} = \frac{|F_1|e^{-j\phi_1}|F_1|e^{j(\phi_1-\Delta\phi)}}{|F_1|^2} = \mathrm{e}^{-j\Delta\phi} \tag{6}$$

where $F^*(u,v)$ means the complex conjugate of $F(u,v)$.

Here we find that the phase of CPS of the two images equals their phase shift and the inverse Fourier transform (IFT) of the CPS is:

$$f_R(x,y) = F^{-1}\{C(u,v)\} = \delta(x-x_0, y-y_0) \tag{7}$$

$f_R(x,y)$ is the displacement response matrix (DRM) of the cloud in images, it is a pulse matrix $\delta(x-x_0, y-y_0)$ in which the element at (x_0, y_0) equals 1 and elements at other coordinates all equal 0. So the displacement vector of two images can be obtained by calculating the CPS and its IFT matrix. Here $x_0 > 0$ means the object in the image moves right and $y_0 > 0$ means moves up.

For actual sky images, because of the presence of an image boundary, the translated grayscale function will "move" partially off the original grid in the time domain when the displacement vector of a cloud is nonzero. In this condition, a periodic extension of the grayscale function based on the periodicity of DFT is required before translation.

3.2 Algorithm procedure of FPCT method

According to the FPCT introduced in section 3.1, the CMDV in two sky images with a certain time interval can be preliminarily calculated according to the followings steps as shown in Figure 3:

(1) Read the grayscale matrix of two sky images: $f_1(x,y)$ and $f_2(x,y)$ for the first and second sky image.

(2) Calculate the Fourier transform of the grayscale matrixes: $F_1(u,v)$ and $F_2(u,v)$ for the first and second sky image.

(3) Calculate the CPS of $F_1(u,v)$ and $F_2(u,v)$: $C(u,v)$.

(4) Calculate the DRM of the cloud images, which is the IFT of the CPS $C(u,v)$: $f_R(x,y) = F^{-1}[C(u,v)]$.

(5) Calculate the CMDV in the sky images according to the coordinate of the highest pulse in the DRM $f_R(x,y)$.

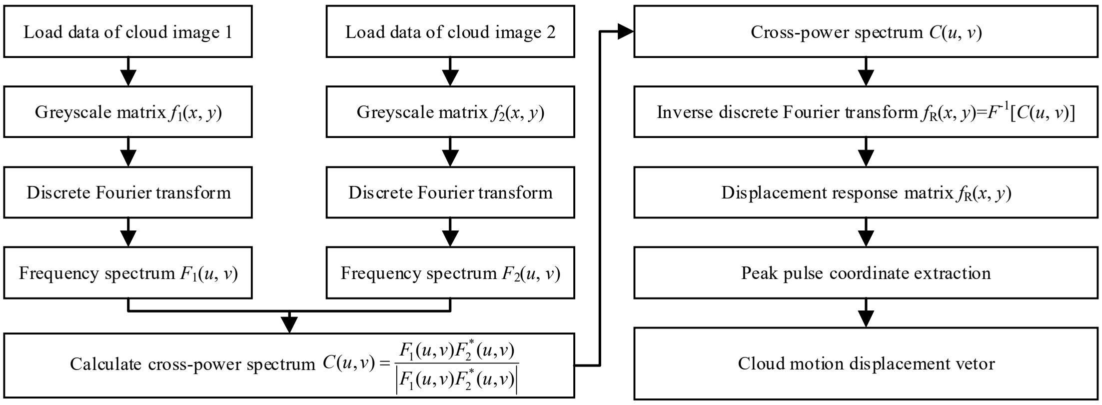

Figure 3. The procedure of CMDV calculation using FPCT.

3.3 Algorithm analysis of FPCT method

According to Section 2.1, the differences between two consecutive sky images separated by a few minutes mainly embody the changes in cloud position and the slight deformation of clouds. In the frequency domain, these differences are manifested as the change of the image phase angle. On the other hand, influenced by cloud thickness, aerosol thickness, and light environment, there may also be a certain global hue difference between different sky images, which will result in a change of the amplitude value in the frequency domain. However, due to the normalization processing in CPS calculations, the inference of hue differences is weakened.

Ideally, when the time interval between two sky images is short enough (e.g. several minutes, depending on the atmosphere conditions), the deformation of clouds is not obvious and all of the cloud pixels move consistently in the images, then the phase of the CPS will be a two-dimensional sinusoidal periodic distribution. In this case, the DRM will be a two-dimensional pulse function distribution, as shown in Figure 4. The highest pulse is located at coordinate $(35, -10)$, other elements in the matrix are considered as noise signals.

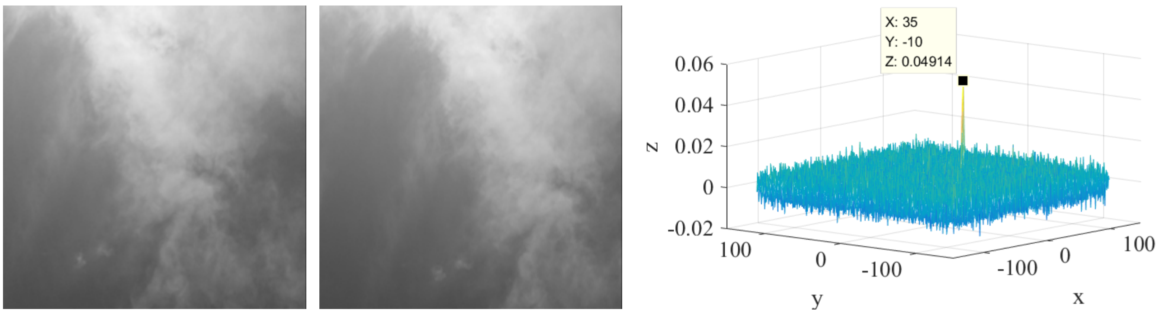

Figure 4. Two-dimensional pulse function distribution, which indicates the cloud moves 35 pixels to the right and moves down 10 pixels in the sky images.

In practice, interference factors such as cloud deformation, changes in solar irradiance, and background clutter are unavoidable. For example, the shape and size of a cloud will change over time; there also may be objects in the image that are stationary or not consistent with cloud motion. Therefore, when we calculate the cloud displacement using actual sky images, ideal cases where sky images only differ by a cloud displacement like shown in Figure 4 are rare. In this situation, the pulse signal that indicates the cloud displacement usually will become less obvious, as shown in Figure 5.

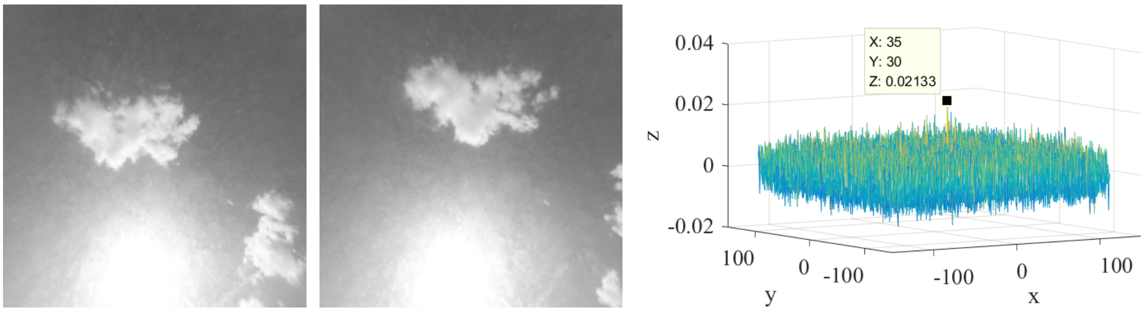

Figure 5. Ambiguous two-dimensional pulse function distribution, which indicates the cloud moves 35 pixels to the right and moves up 30 pixels in the sky images.

All the objects in images are composed of pixels, and the deformation of cloud shape and noise signals in CPSs can be considered as the reflection of inconsistent movements of pixels in sky images. In order to study this effect, we set up a simple example. Assuming that there are two objects 'a' and 'b' moving independently in an image and the background pixels all have value 0, the displacement vector of object 'a' is (x_a, y_a) and the displacement vector of object 'b' is (x_b, y_b), as shown in Figure 6.

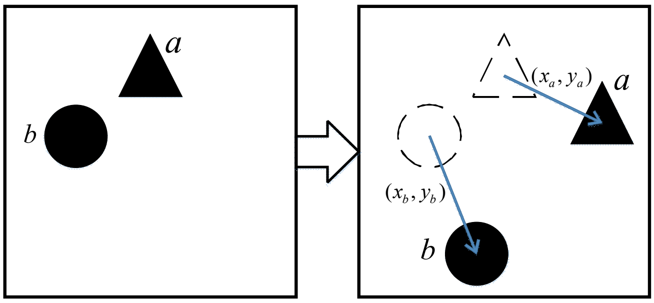

Figure 6. Two objects that moving independently in one image

Then $f_1(x,y)$, the image before displacement, and $f_2(x,y)$, the image after, can be decomposed as:

$$f_1(x,y)=f_{1.a}(x,y)+f_{1.b}(x,y) \tag{8}$$

$$f_2(x,y)=f_{2.a}(x,y)+f_{2.b}(x,y)=f_{1.a}(x-x_a,y-y_a)+f_{1.b}(x-x_b,y-y_b) \tag{9}$$

where the first subscript of '1' or '2' denotes the image, the second subscript of 'a' or 'b' denotes the object.

According to Equations (1) to (4), there will be:

$$F_{2.a}(u,v)=F_{1.a}(u,v)e^{-\mathrm{j}2\pi(\frac{ux_a}{M}+\frac{vy_a}{N})}=\left|F_{1.a}\right|e^{-j[\phi_{1.a}+2\pi(\frac{ux_a}{M}+\frac{vy_a}{N})]}=\left|F_{1.a}\right|e^{-j(\phi_{1.a}-\Delta\phi_a)} \tag{10}$$

$$F_{2.b}(u,v)=F_{1.b}(u,v)e^{-\mathrm{j}2\pi(\frac{ux_b}{M}+\frac{vy_b}{N})}=\left|F_{1.b}\right|e^{-j[\phi_{1.b}+2\pi(\frac{ux_b}{M}+\frac{vy_b}{N})]}=\left|F_{1.b}\right|e^{-j(\phi_{1.b}-\Delta\phi_b)} \tag{11}$$

Then the Fourier transforms of $f_1(x,y)$ and $f_2(x,y)$ are:

$$F_1(u,v)=F_{1.a}(u,v)+F_{1.b}(u,v)=\left|F_{1.a}\right|e^{-j\phi_{1.a}}+\left|F_{1.b}\right|e^{-j\phi_{1.b}} \tag{12}$$

$$F_2(u,v)=F_{2.a}(u,v)+F_{2.b}(u,v)=\left|F_{1.a}\right|e^{-j[\phi_{1.a}-\Delta\phi_a]}+\left|F_{1.b}\right|e^{-j[\phi_{1.b}-\Delta\phi_b]} \tag{13}$$

Calculate the CPS:

$$\begin{aligned}C(u,v)&=\frac{F_1(u,v)F_2^*(u,v)}{\left|F_1(u,v)F_2^*(u,v)\right|}=\frac{[\left|F_{1.a}\right|e^{-j\phi_{1.a}}+\left|F_{1.b}\right|e^{-j\phi_{1.b}}]}{\left|F_1\right|\left|F_2\right|}\cdot\frac{[\left|F_{1.a}\right|e^{-j(\Delta\phi_a-\phi_{1.a})}+\left|F_{1.b}\right|e^{-j(\Delta\phi_b-\phi_{1.b})}]}{\left|F_1\right|\left|F_2\right|}\\&=\frac{\left|F_{1.a}\right|^2e^{-j\Delta\phi_a}+\left|F_{1.b}\right|^2e^{-j\Delta\phi_b}}{\left|F_1\right|\left|F_2\right|}+\frac{\left|F_{1.a}\right|\left|F_{1.b}\right|[e^{-j(\phi_{1.a}-\phi_{1.b}+\Delta\phi_b)}+e^{-j(\phi_{1.b}-\phi_{1.a}+\Delta\phi_a)}]}{\left|F_1\right|\left|F_2\right|}\end{aligned} \tag{14}$$

According to the linear property and convolution theorem duality of Fourier transform and its inverse:

$$F[a \cdot f_1(x,y) + b \cdot f_2(x,y)] = a \cdot F[f_1(x,y)] + b \cdot F[f_2(x,y)] \tag{15}$$

$$F[f_1(x,y) * f_2(x,y)] = F[f_1(x,y)] \cdot F[f_2(x,y)] \tag{16}$$

where $f_1(x,y) * f_2(x,y)$ means the convolution of $f_1(x,y)$ and $f_2(x,y)$.

The DRM calculated by inverse Fourier transform of $C(u,v)$ is:

$$\begin{aligned} f_R(x,y) &= F^{-1}[C(u,v)] = F^{-1}\{\frac{|F_{1.a}|^2 e^{-j\Delta\phi_a}}{|F_1||F_2|}\} + F^{-1}\{\frac{|F_{1.b}|^2 e^{-j\Delta\phi_b}}{|F_1||F_2|}\} + F^{-1}\{\frac{|F_{1.a}||F_{1.b}|[e^{-j(\phi_{1.a}-\phi_{1.b}+\Delta\phi_b)} + e^{-j(\phi_{1.b}-\phi_{1.a}+\Delta\phi_a)}]}{|F_1||F_2|}\} \\ &= \delta(x-x_a, y-y_b) * F^{-1}\left\{\frac{|F_{1.a}|^2}{|F_1||F_2|}\right\} + \delta(x-x_b, y-y_b) * F^{-1}\left\{\frac{|F_{1.b}|^2}{|F_1||F_2|}\right\} + F^{-1}\{\frac{|F_{1.a}||F_{1.b}|[e^{-j(\phi_{1.a}-\phi_{1.b}+\Delta\phi_b)} + e^{-j(\phi_{1.b}-\phi_{1.a}+\Delta\phi_a)}]}{|F_1||F_2|}\} \end{aligned} \tag{17}$$

According to function (17), $f_R(x,y)$ consists three parts:

(1) $\delta(x-x_a, y-y_a) * F^{-1}\left\{\frac{|F_{1.a}|^2}{|F_1||F_2|}\right\}$;

(2) $\delta(x-x_b, y-y_b) * F^{-1}\left\{\frac{|F_{1.b}|^2}{|F_1||F_2|}\right\}$;

(3) $F^{-1}\{\frac{|F_{1.a}||F_{1.b}|[e^{-j(\phi_{1.a}-\phi_{1.b}+\Delta\phi_b)} + e^{-j(\phi_{1.b}-\phi_{1.a}+\Delta\phi_a)}]}{|F_1||F_2|}\}$.

According to the definition of convolution, the convolution of matrixes $f_1(x,y)$ and $f_2(x,y)$ can be calculated as:

$$h(x,y) = f_1(x,y) * f_2(x,y) = \sum_{m=0}^{M-1}\sum_{n=0}^{N-1} f_1(m,n) \cdot f_2(x-m, y-n) \tag{18}$$

For part (1) of $f_R(x,y)$, there will be:

$$f_1(x,y) = \delta(x-x_a, y-y_a) \tag{19}$$

$$f_2(x,y) = F^{-1}\left\{\frac{|F_{1.a}|^2}{|F_1||F_2|}\right\} \tag{20}$$

Here $f_1(x,y)$ equals 1 only when $x = x_a$ and $y = y_a$. In other cases, the values of $f_1(x,y)$ are all 0. Then based on function (18), there will be:

$$\delta(x-x_a, y-y_a) * F^{-1}\left\{\frac{|F_{1.a}|^2}{|F_1||F_2|}\right\} = f_2(x-x_a, y-y_a) \tag{21}$$

where $f_2(x,y) = F^{-1}\left\{\frac{|F_{1.a}|^2}{|F_1||F_2|}\right\}$ which means the result of the convolution calculation is the translation of $F^{-1}\left\{\frac{|F_{1.a}|^2}{|F_1||F_2|}\right\}$ by a displacement of (x_a, y_a).

According to the IFT function:

$$f(x,y) = \frac{1}{MN}\sum_{u=0}^{M-1}\sum_{v=0}^{N-1} F(u,v) e^{j2\pi(\frac{ux}{M}+\frac{vy}{N})} \tag{22}$$

where x, y are the variables of coordinate variables in the original image and u, v are the coordinate variables in the Fourier transform of the original image.

As $\frac{|F_{1.a}|^2}{|F_1||F_2|}$ is a real matrix, the maximum value of its IFT matrix $F^{-1}\left\{\frac{|F_{1.a}|^2}{|F_1||F_2|}\right\}$ is located at $(0,0)$. Then by the convolution calculation with $\delta(x-x_a, y-y_a)$, the maximum value will move to (x_a, y_a).

Therefore, the first two parts of DRM $f_R(x,y)$ will show up as a peak pulse located at (x_a, y_a) and (x_b, y_b) respectively. While for the third part, which is the interaction term between object 'a' and object 'b', will be represented as the erratic noise signal because $\emptyset_{1.a}$ and $\emptyset_{1.b}$ usually comprise a plurality of components.

Based on the above calculations and the linear property of Fourier transforms, the introduction of new objects moving in new directions in the images will also introduce new pulses and more noise signals in the DRM. The following conclusions can be drawn [43,44]:

(1) The displacement of an object in two images will introduce a pulse at the coordinate corresponding to the displacement in the IFT matrix of CPS.

(2) If multiple objects are moving independently in the images, then multiple pulses corresponding to the displacements of each object will be introduced as well. The amplitude of each pulse is proportional to the number of pixels of the moving object but will be smaller because the sum value of all the elements in DRM is constant.

(3) In any situation, there will always be background noise signals evenly distributed throughout the DRM, including the interaction between multiple objects and the original image noise.

(4) For sky images, there may be three cases:

(A) Ideal case: the cloud shape is unchanged during movement, thus all the cloud pixels move at a uniform speed, the pulse corresponding to cloud displacement will be quite visible in the DRM.

(B) Not ideal but acceptable case: if the deformation of clouds is occurring with cloud movement, we may get a DRM combined with multiple less obvious pulses, but the peak pulse corresponding to the cloud movement vector can still be distinguished from the noise.

(C) The worst case: the pulse amplitude will be smaller than the noise signals and cause the algorithm to be invalid.

According to the algorithm of cloud displacement estimation, the calculated CMDV in two consecutive sky images will be the coordinate of the highest point in the IFT matrix of CPS. However, as the algorithm analysis part shows, the accuracy and credibility of the result cannot be guaranteed under all circumstances.

4 IPSI based cloud motion displacement vector calculation

So far, it is still terrifically complex and difficult to mathematically describe and model the cloud motion process, not to speak of the deformation estimation of clouds and the specific influence analysis on FPCT based CMDV calculation methods. Therefore, to improve the accuracy and reliability, we proposed an IPSI based CMDV calculation method using FPCT for minute time scale solar irradiance forecasting. First, the IPSI in terms of the synchronous rotation of two images is expounded to reflect the invariable cross correlation characteristic on the image displacement of two different images in frequency domain. Second, multiple CMDVs are obtained from the corresponding consecutive image pairs according to different rotational angles compared to the original images using FPCT. At last, the final CMDV is generated from all of the calculated CMDVs through a density and distance distribution based centroid iteration algorithm.

4.1 Phase shift invariance in image transformation

When using actual sky images to calculate the CMDV, usually two factors can lead to erroneous results. The first is the pixels of still objects in sky images such as sun pixels and sky background pixels. The displacement of these objects in a sky image is almost zero, which means they will introduce pulses located around the coordinate $(0,0)$. Normally these pulse signals can be removed by filtering. The second factor is cloud deformation, which may introduce multiple pulses located at different coordinates. Usually, the amplitude of these pulses is smaller than that of the pulse corresponding to CMDV. Both factors can reduce the height of the pulse corresponding to CMDV and decrease the credibility of the results. Therefore, in CMDV calculation, if the amplitude of the pulse signal corresponding to cloud displacement is larger than all the other signals, the calculated result will be correct. Otherwise, the pulse signal will be below the level of the background noise.

In summary, for CMDV calculation using FPCT, there is a probability of P% leading to a correct result and a probability of (1-P)% leading to an incorrect random result. The specific value of P depends on the sample images.

Based on the above analysis, suppose there is a transformation h for grayscale matrix $f(x,y)$ and the transformed matrix is $f'(x,y)$, that is:

$$f'(x,y) = h[f(x,y)] \tag{23}$$

For two consecutive image $f_1(x,y)$ and $f_2(x,y)$ that differ by a displacement (x_0,y_0), their transformed version are $f_1'(x,y)$ and $f_2'(x,y)$ according to the transformation h. If the phase shift between $f_1(x,y)$ and $f_2(x,y)$ is invariance before and after the transformation, we can calculate the displacement vector (x_0,y_0) using the transformed image as well.

Using a series of such transformations that satisfying the phase shift invariant condition, we can calculate a series of displacement vectors. The calculation results will not all be the same due to the transformation of sample images. However, according to statistical theory and the summary that there is a probability of P% leading to a correct result and a probability of (1-P)% leading to an incorrect random result of FPCT, about P% of the results should be correct and very close to each other while other results are just random vectors. Therefore, we can obtain the final correct displacement vector according to the distribution of all the calculated vectors using transformed images.

One of the simplest and easiest transformations of an image is rotation. For two consecutive image $f_1(x,y)$ and $f_2(x,y)$ that only differ by a displacement, their rotation transformed version are $f_1'(x,y)$ and $f_2'(x,y)$ as shown in Figure 7, then

$$f_1'(x,y) = f_1(x\cos\theta + y\sin\theta, -x\sin\theta + y\cos\theta) \tag{24}$$

$$f_2'(x,y) = f_2(x\cos\theta + y\sin\theta, -x\sin\theta + y\cos\theta) \tag{25}$$

where the rotation angle $\theta = 30°$.

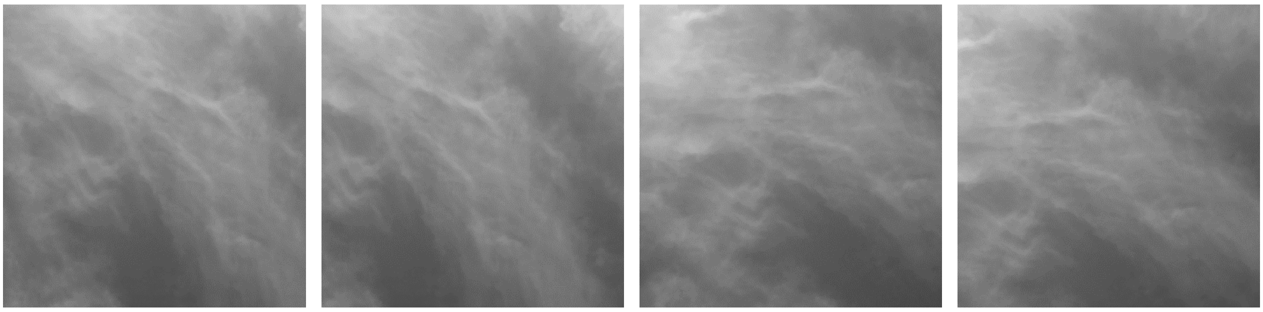

(a) (b) (c) (d)

Figure 7. The sample images in function (24) and (25). (a) Image of $f_1(x,y)$. (b) Image of $f_2(x,y)$. (c) Image of $f_1'(x,y)$. (d) Image of $f_2'(x,y)$.

According to the Fourier rotation property, rotating an image $f(x,y)$ by an angle θ rotates its Fourier transformation $F(u,v)$ by the same angle. Conversely, rotating $F(u,v)$ rotates $f(x,y)$ by the same angle. Therefore, the phase spectrum of cross-power matrix calculated using rotated images $f_1'(x,y)$, $f_2'(x,y)$ will also be a rotated version of that calculated using the original images $f_1'(x,y)$, $f_2'(x,y)$, as shown in Figure 8.

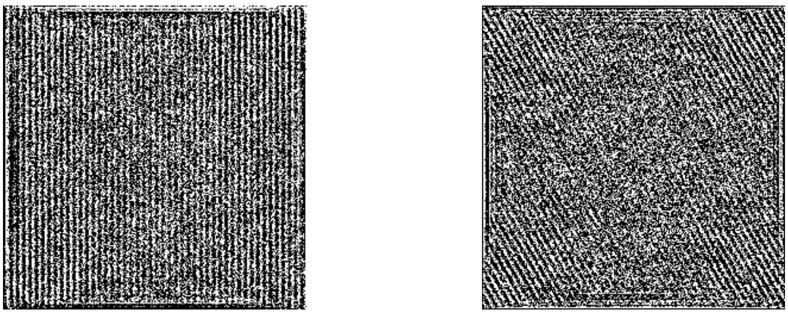

(a) (b)

Figure 8. The phase spectrum of cross-power matrix. (a) Calculated using original images. (b) Calculated using rotated images.

Then the calculated displacement vector using rotated sky images will also rotate by the angle θ. If the displacement vector in actual sky images is (x_0, y_0) and the vector in images rotated by θ is (x_θ, y_θ), then

$$\begin{aligned} x_0 &= x_\theta \cos\theta + y_\theta \sin\theta \\ y_0 &= -x_\theta \sin\theta + y_\theta \cos\theta \end{aligned} \tag{26}$$

This means the phase shifts that corresponding to displacement vectors between the original images and rotated images are essentially the same, the difference as shown in Figure 8 is only due to the change in observation angles.

Therefore, rotation is a kind of image transformation that satisfies the image phase shift invariance condition. Let the value of θ change incrementally from $0°$ to $90°$, then we can calculate the CMDVs in rotated sky images corresponding to all of the rotation angles and obtain the actual displacement vectors in the original images according to function (26). Due to the IPSI in image rotation process, all the calculated actual displacement vectors should be invariant whatever the rotation angle may be.

4.2 CMDV calculation based on IPSI and centroid iteration

In this section, we proposed an IPSI based CMDV calculation method using FPCT for minute time scale solar irradiance forecasting. The method consists of two main parts: multiple CMDV calculations based on the IPSI characteristic and the final CMDV generation through centroid iteration strategy.

To calculate the CMDV utilizing the IPSI characteristic in image deformation, we rotate each sky image continuously from 0° to 90° with a certain angle each time and extract the corresponding processing region. When the total rotation angle is equal to or greater than 90°, the elements of the extracted image grayscale matrix would be the same with the existing matrices, just arranged in a different direction, such as the gray scale matrix rotated 90° and the original gray scale matrix. Figure 9 shows an example with rotation angle of 30°.

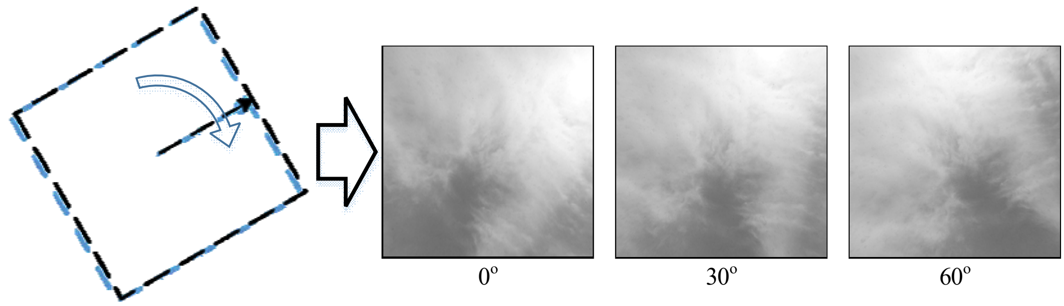

Figure 9. Rotate the sky image by 30° each time and extract the processing region.

Let the rotation angle be R, then we can obtain 90/R pair of sky images and the same number of CMDVs by multiple calculations (90 should be divisible by R).

The coordinates of CMDVs for each rotation would be:

$$D = \{(x_1, y_1), (x_2, y_2), \cdots, (x_n, y_n)\}$$
$$n = \frac{90}{R} \tag{27}$$

To obtain the final CMDV based on D and reduce random noise, we propose the following centroid iteration based calculation process as shown in Figure 10:

1) Calculate the average of all the CMDVs in D:

$$D_{ave} = \left(\frac{1}{n}\sum_{i=1}^{n} x_i, \frac{1}{n}\sum_{i=1}^{n} y_i\right) \tag{28}$$

2) Calculate the distance between D_{ave} and each vector in D, and then remove the farthest vector from D.

3) Calculate the new average D_{ave}' according to function (28) and the relative distance between D_{ave} and D_{ave}':

$$d = \frac{|D_{ave} - D_{ave}'|}{|D_{ave}|} \tag{29}$$

4) Set a threshold value ε. If $d > \varepsilon$, let $D_{ave} = D_{ave}'$ and repeat the step 2) and step 3), otherwise stop the iteration process. Here the value of the threshold ε will affect the number and concentration level of residual CMDVs after centroid iteration and usually can be determined according to image size and experiments using historical data.

5) The final value of D_{ave} will be the calculated CMDV.

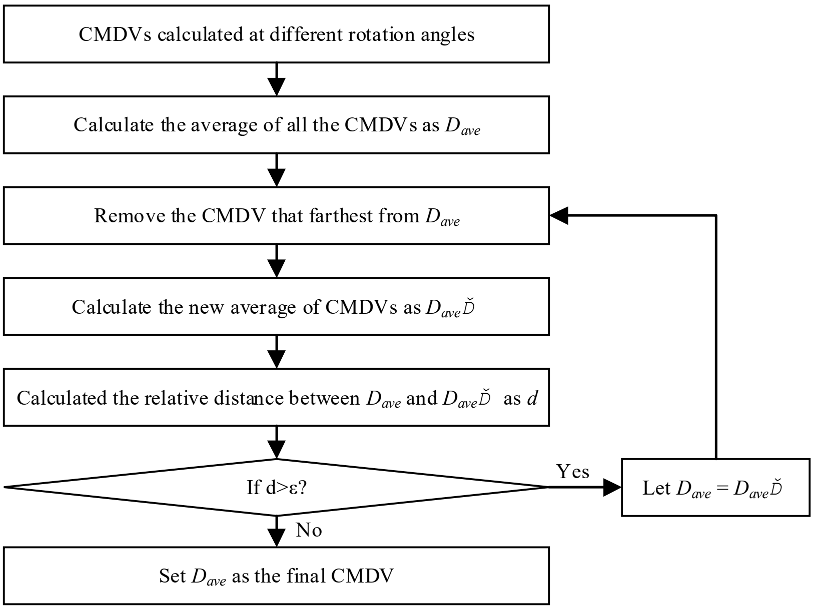

Figure 10. Centroid iteration process.

5 Simulation and discussion

5.1 Simulation design and data resources

In this part, to test and evaluate the performance of proposed IPSI-based method, multiple algorithms including some well-established works in existing literature and the proposed method will be applied to calculate CMDVs of a series of continuous sky images. Detail information in the calculation process are displayed and analyzed in section 5.2.

Considering two scenarios of thick clouds and thin clouds, we chose two sequences of sky images for simulation: sequence A shows the motion of thick clouds and sequence B shows the motion of thin clouds. The deformation of clouds in sequence A is also more obvious than in sequence B. Both sequences contain 50 continuous sky images and the 1st, 25th, and 50th sky images of the two image sequences are shown in Figure 11. The resolution of each sky image is 513×513 pixels.

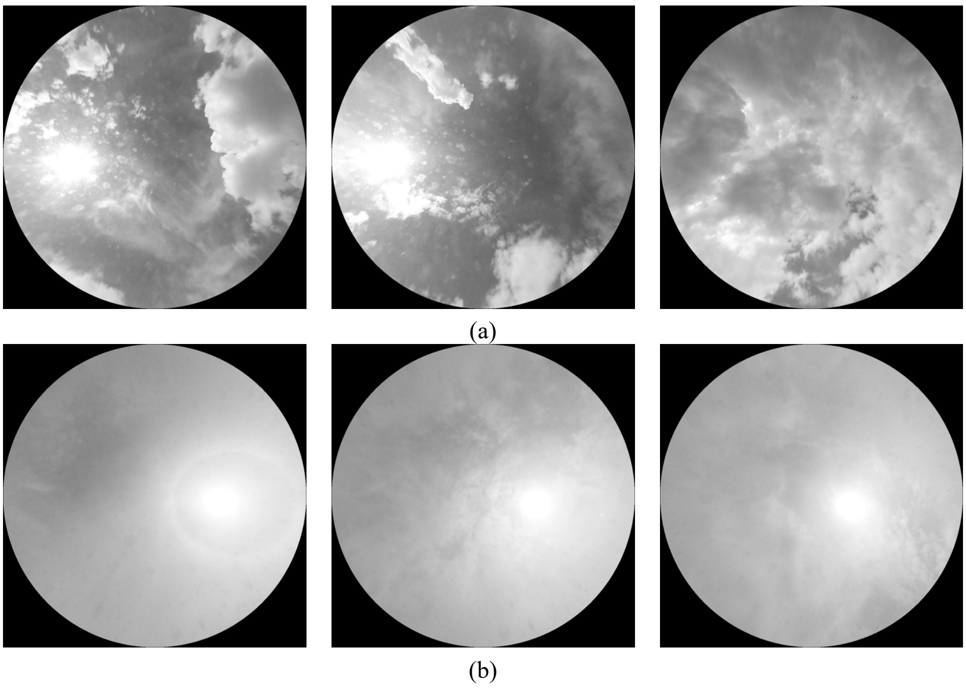

Figure 11. (a) Sky image sequence A reflects the motion of thick clouds. (b) Sky image sequence B shows the motion of thin clouds.

5.2 Simulation results and comparison

Four displacement estimation methods are applied in our simulations to calculate the cloud displacement:

(1) The original FPCT based CMDV calculation method, which calculates the IFT matrix of CPS directly and considers the coordinates of the highest pulse signal as cloud displacement.

(2) The IPSI-based CMDV calculation method using FPCT proposed in this paper.

(3) The PIV method contained in the MATLAB toolbox ‘MPIV’, which was developed by Mori and Chang [45]. This method is also applied in [15] to calculate cloud velocity.

(4) The OF method using Piotr's Computer Vision MATLAB Toolbox [46].

Sky image sequences A and B both contain 50 consecutive sky images and the CMDVs between consecutive sky images are calculated by the above four methods. Therefore, 49 CMDVs for each method are obtained in one image sequence, and the displacement calculation results in the X- coordinate and Y- coordinate are shown in Figure 12 and Figure 17, respectively.

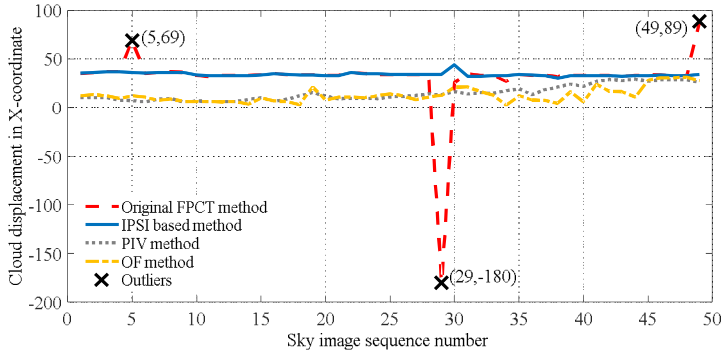

(a)

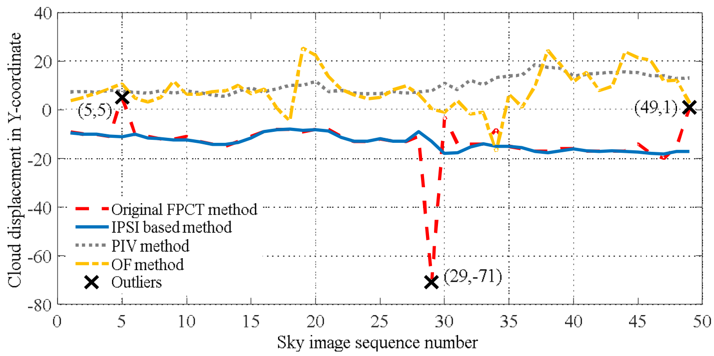

(b)

Figure 12. CMDVs in sky image sequence A. (a) The displacement in the X-coordinate. (b) The displacement in the Y-coordinate.

In Figure 12, we can see that most of the results of the original FPCT method and the proposed IPSI-based method are the same. Then we can first draw a simple conclusion: during the period of the sky image sequence A, the displacements in the X-coordinate vary around 35pixels and the displacements in the Y-coordinate vary around -13pixels. However, the 5th, 29th, and 49th results obtained by original FPCT method are inconsistent with the average movement of clouds, the CMDVs of these 3 outliers are (69, 5), (-180, -71), and (89, 1). Taking the 5th result as an example, the IFT matrix of CPS between the 5th and 6th sky images is shown in Figure 13. It can be seen that the highest pulse is located at (69, 5), as shown in Figure 12, higher than the pulse located at (37, -9), which is a more credible result when examining the total displacements of clouds in all 50 sky images in sequence A.

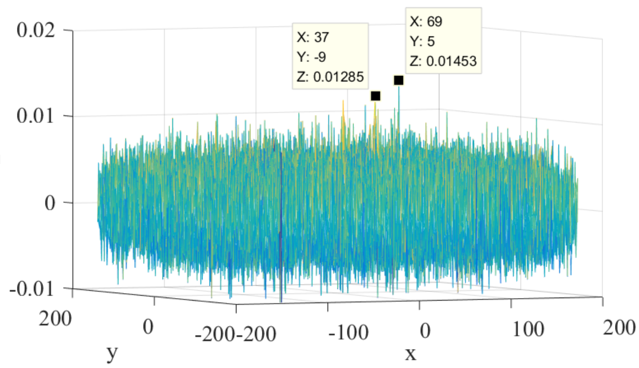

Figure 13. The DRM between the 5th and 6th sky images in sequence A.

Then the proposed IPSI-based CMDV calculation method is applied to correct this result. Theoretically, the rotation angle should be smaller enough to provide sufficient calculated displacement vectors for iterative calculations. However, excessive vectors are not conducive to improving the accuracy according to simulations. Considering the computational complexity, we set the angle of each rotation to 1°. The threshold value for *d* in function (23) will affect the number and concentration level of residual CMDVs after the centroid iterations. Here we set the threshold $\varepsilon = 0.01$ according to historical data and experiments. The results of the proposed method are shown in Figure 14 and the final CMDV is (36.43, -9).

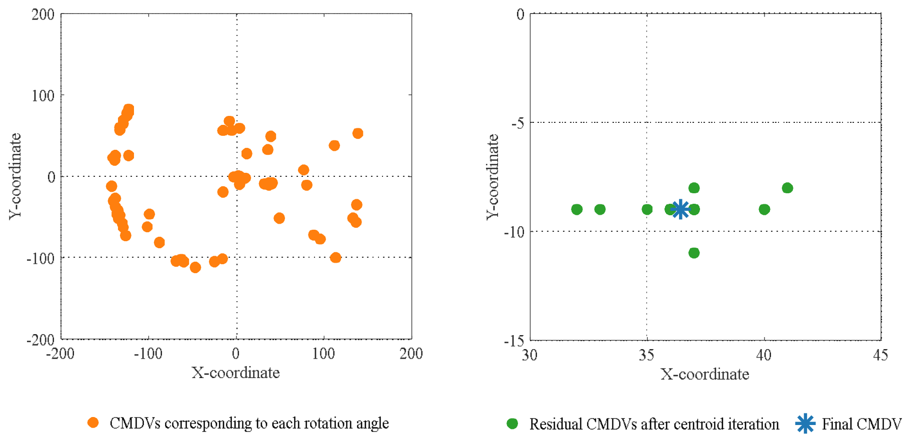

(a) (b)

Figure 14. The calculation results of CMDV. (a) CMDVs corresponding to each rotation (90 vectors). (b) Final result of CMDV after centroid iteration.

The 29th and 49th results are shown in Figure 15. The final CMDVs calculated by the proposed method are (33.89, -12.78) and (31, -16). It can be seen that all three outliers obtained by the original FPCT method are corrected by the proposed IPSI-based CMDV calculation method.

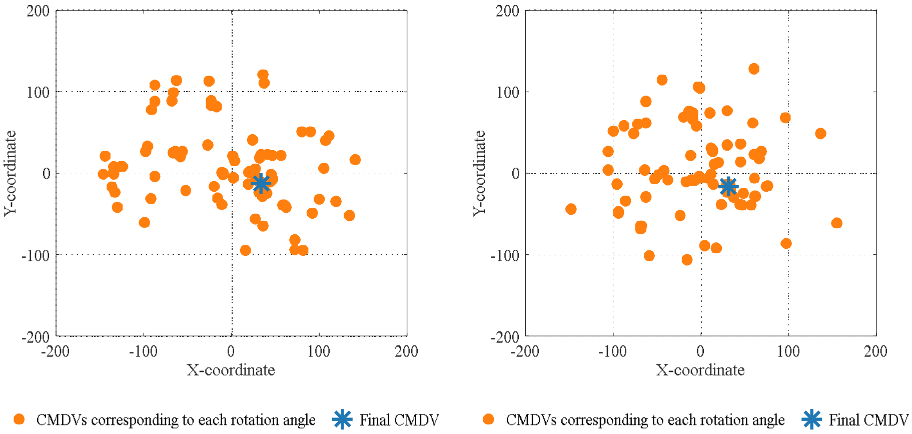

Figure 15. The 29th (left) and 49th (right) calculation results of CMDV.

The CMDVs in the X-coordinate obtained by the PIV method are the same as our proposed method in direction but the displacement distance is shorter. While in the Y-coordinate, according to the PIV method the clouds in sky images are moving up, but according to FPCT-based method, the clouds should be moving down. This disagreement between the two methods is particularly pronounced when dealing with the last several sky images.

In this research, sky images are the only means of cloud observation, and we can only obtain the motion information of clouds according to the images. Therefore, to evaluate the accuracy of a calculation result of CMDV, it is necessary to combine the CMDVs calculated using other sky images that are close in time and artificial observations.

The last four sky images in image sequence A are shown in Figure 16, and it can be seen that the sky region at the bottom of the image is becoming smaller and the thick cloud region at the top of the image is expanding, which indicates that the clouds are moving from top to bottom of the image. It is also noticeable that a small piece of cloud marked by the blue circle is moving to the lower right of the image. Therefore, according to the above observations, the value of CMDV in the Y-coordinate should be less than zero, and the results obtained by IPSI based method are more reasonable.

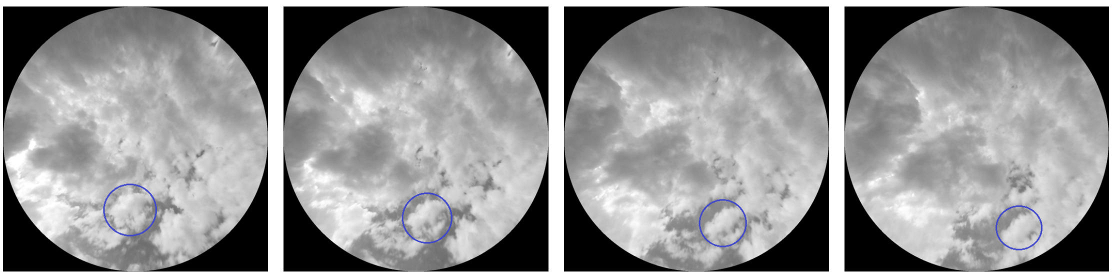

Figure 16. The last four sky images in image sequence A.

The calculated CMDVs using OF method are close to PIV's results. However, as the cloud brightness may be changed according whether the sun is blocked or not, the results of OF method is not as stable as that of PIV method.

In Figure 17, the CMDV calculation results of first three methods are consistent in directions, i.e. clouds moving up and right in the sky images. The results of the original FPCT method and the IPSI-based method are practically identical in image sequence B, and very stable compared with the PIV method. For thin clouds, the gray scale value of cloud pixel is strongly influenced by sunlight and could change obviously during the cloud movement. Therefore, the prerequisite assumption of OF method is not satisfied, so the CMDVs results calculated by this method are unacceptable.

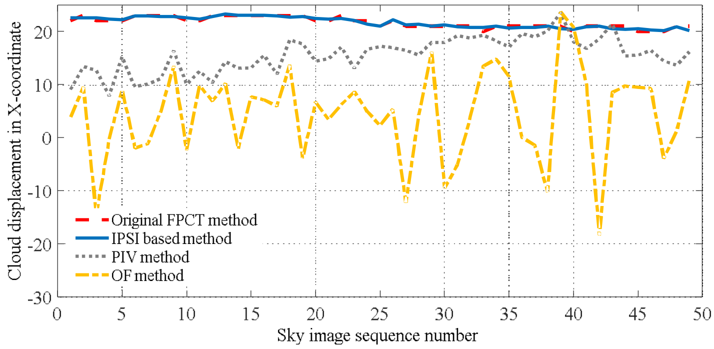

(a)

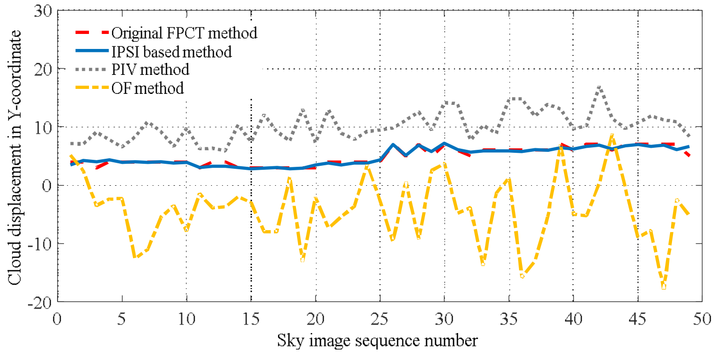

(b)

Figure 17. CMDVs in sky image sequence B. (a) The displacement in the X-coordinate. (b) The displacement in the Y-coordinate.

5.3 Discussion

Due to the cloud deformation and brightness changes in sky images, there is not yet an effective method to judge the accuracy of CMDVs. However, cloud movement is a reflection of atmospheric physical movement processes, and presumably because of inertia, the displacement obtained by consecutive sky image pairs should usually be similar. Based on the above considerations, the performance and effectiveness of the proposed IPSI-based CMDV calculation method are validated by the simulation results, because this method not only produces a more accurate output than the original FPCT method but also can achieve more stable results compared with PIV and OF methods.

Theoretically, the PIV and OF method focuses on the specific local/regional details of image pixels. The PIV and OF based CMDV calculation are part-to-whole methods, which means they can provide more detail image information and more likely to be disturbed by local deformation or noise signals of the image. While for FPCT method, the global trends of clouds in sky images are more concerned, so local deformation and noise signals can hardly affect the CMDV calculation results. Additionally, the IPSI-based method is more robust than FPCT method, as the image transformation and centroid iteration processing further weakened the influence of deformation and noise signal.

6 Conclusions

According to the essential characteristics analysis on the displacements of two sky images, an IPSI based CMDV calculation method using FPCT for minute time scale solar irradiance forecasting is proposed to improve the performance of CMDV calculation method. The proposed IPSI based CMDV calculation method overcomes the shortcomings of insufficient reliability of original FPCT method, thus improved the availability of FPCT method in CMDV calculation approach. Actual sky image data is used to verify the effectiveness of proposed method. The comparison in simulation shows that the performance of IPSI based CMDV calculation method is better than two commonly used gray scale information based methods (PIV and OF). In addition, the proposed method in this paper did not increase much work load in the algorithm process, so that the merits of FPCT method such as easy to program and high calculation speed remain, which makes it easy to utilize the IPSI based CMDV calculation method into practical applications.

The future works base on this research will be carried out mainly focus on three following aspects: (1) More comparisons on larger dataset to further validate the proposed IPSI-based method in various complex cases; (2) Utilize the proposed method associate with "Sky image-Surface irradiance" mapping model to establish a stepwise accurate surface solar irradiance forecasts method; (3) Related researches in terms of methodological improvements on the sky image based ultra short-term solar irradiance forecasting.

Acknowledgments: This work was supported in part by the National Natural Science Foundation of China (grant No. 51577067), the Beijing Natural Science Foundation of China (grant No. 3162033), the Hebei Natural Science Foundation of China (grant No. E2015502060), the State Key Laboratory of Alternate Electrical Power System with Renewable Energy Sources (grant No. LAPS16007, LAPS16015), the Science & Technology Project of State Grid Corporation of China (SGCC), the Open Fund of State Key Laboratory of Operation and Control of Renewable Energy & Storage Systems (China Electric Power Research Institute) (No.5242001600FB), the China Scholarship Council. This work was also supported by the U.S. Department of Energy under Contract No. DE-AC36-08-GO28308 with the National Renewable Energy Laboratory. M. Shafie-khah and João P. S. Catalão acknowledge the support by FEDER funds through COMPETE 2020 and by Portuguese funds through FCT, under Projects SAICT-PAC/0004/2015-POCI-01-0145-FEDER-016434, POCI-01-0145-FEDER-006961, UID/EEA/50014/2013, UID/CEC/50021/2013, and UID/EMS/00151/2013, and also funding from the EU 7th Frame-work Programme FP7/2007–2013 under GA No. 309048.

References

[1] REN21. Renewables 2016 Global Status Report. 2016.

[2] International Energy Agency. Renewables Information 2017. OECD Publishing; 2017.

[3] Osório GJ, Lujano-Rojas JM, Matias JCO, Catalão JPS. A fast method for the unit scheduling problem with significant renewable power generation. Energy Convers Manag 2015;94:178–89. doi:10.1016/j.enconman.2015.01.071.

[4] Cui M, Zhang J, Hodge B-M, Lu S, Hamann HF. A Methodology for Quantifying Reliability Benefits from Improved Solar Power Forecasting in Multi-Timescale Power System Operations. IEEE Trans Smart Grid 2017:1–1. doi:10.1109/TSG.2017.2728480.

[5] Wang F, Xu H, Xu T, Li K, Shafie-khah M, Catalão JPS. The values of market-based demand response on improving power system reliability under extreme circumstances. Appl Energy 2017;193:220–31. doi:10.1016/j.apenergy.2017.01.103.

[6] Chen Q, Wang F, Hodge B-M, Zhang J, Li Z, Shafie-khah M, et al. Dynamic Price Vector Formation Model Based Automatic Demand Response Strategy for PV-assisted EV Charging Station. IEEE Trans Smart Grid 2017; 8(6): 2903–2915. doi:10.1109/TSG.2017.2693121.

[7] Rana M, Koprinska I, Agelidis VG. Univariate and multivariate methods for very short-term solar photovoltaic power forecasting. Energy Convers Manag 2016;121:380–90. doi:10.1016/j.enconman.2016.05.025.

[8] Wang F, Zhen Z, Mi Z, Sun H, Su S, Yang G. Solar irradiance feature extraction and support vector machines based weather status pattern recognition model for short-term photovoltaic power forecasting. Energy Build 2015;86:427–38. doi:10.1016/j.enbuild.2014.10.002.

[9] Urraca R, Antonanzas J, Alia-Martinez M, Martinez-De-Pison FJ, Antonanzas-Torres F. Smart baseline models for solar irradiation forecasting. Energy Convers Manag 2016;108:539–48. doi:10.1016/j.enconman.2015.11.033.

[10] Wang F, Mi Z, Su S, Zhao H. Short-term solar irradiance forecasting model based on artificial neural network using statistical feature parameters. Energies 2012;5:1355–70. doi:10.3390/en5051355.

[11] Quesada-Ruiz S, Chu Y, Tovar-Pescador J, Pedro HTC, Coimbra CFM. Cloud-tracking methodology for intra-hour DNI forecasting. Sol Energy 2014;102:267–75. doi:10.1016/j.solener.2014.01.030.

[12] Jiang H, Dong Y. Forecast of hourly global horizontal irradiance based on structured Kernel Support Vector Machine: A case study of Tibet area in China. Energy Convers Manag 2017;142:307–21. doi:10.1016/j.enconman.2017.03.054.

[13] Azimi R, Ghayekhloo M, Ghofrani M. A hybrid method based on a new clustering technique and multilayer perceptron neural networks for hourly solar radiation forecasting. Energy Convers Manag 2016;118:331–44. doi:10.1016/j.enconman.2016.04.009.

[14] Jiang H, Dong Y. A nonlinear support vector machine model with hard penalty function based on glowworm swarm optimization for forecasting daily global solar radiation. Energy Convers Manag 2016;126:991–1002. doi:10.1016/j.enconman.2016.08.069.

[15] Marquez R, Coimbra CFM. Intra-hour DNI forecasting based on cloud tracking image analysis. Sol Energy 2013;91:327–36. doi:10.1016/j.solener.2012.09.018.

[16] Zhang J, Hodge B, Lu S, Hamann HF, Lehman B, Simmons J, et al. Baseline and target values for regional and point PV power forecasts : Toward improved solar forecasting. Sol Energy 2015;122:804–19. doi:10.1016/j.solener.2015.09.047.

[17] Wolff B, Kühnert J, Lorenz E, Kramer O, Heinemann D. Comparing support vector regression for PV power forecasting to a physical modeling approach using measurement, numerical weather prediction, and cloud motion data. Sol Energy 2016;135:197–208. doi:10.1016/j.solener.2016.05.051.

[18] Peng Z, Yu D, Huang D, Heiser J, Kalb P. A hybrid approach to estimate the complex motions of clouds in sky images. Sol Energy 2016;138:10–25. doi:10.1016/j.solener.2016.09.002.

[19] Kurtz B, Kleissl J. Measuring diffuse, direct, and global irradiance using a sky imager. Sol Energy 2017;141:311–22. doi:10.1016/j.solener.2016.11.032.

[20] Alonso-Montesinos J, Batlles FJ, Portillo C. Solar irradiance forecasting at one-minute intervals for different sky conditions using sky camera images. Energy Convers Manag 2015;105:1166–77. doi:10.1016/j.enconman.2015.09.001.

[21] Lowe DG. Object recognition from local scale-invariant features. Proc. Seventh IEEE Int. Conf. Comput. Vis., 1999, p. 1150–7 vol.2. doi:10.1109/ICCV.1999.790410.

[22] Lourenco M, Barreto JP, Vasconcelos F. SRD-SIFT: Keypoint detection and matching in images with radial distortion. IEEE Trans Robot 2012;28:752–60. doi:10.1109/TRO.2012.2184952.

[23] Cheng HY. Cloud tracking using clusters of feature points for accurate solar irradiance nowcasting. Renew Energy 2017;104:281–9. doi:10.1016/j.renene.2016.12.023.

[24] Barron JL, Fleet DJ, Beauchemin SS. Performance of optical flow techniques. Int J Comput Vis 1994;12:43–77. doi:10.1007/BF01420984.

[25] Sun D, Roth S, Lewis JP, Black MJ. Learning optical flow. Lect. Notes Comput. Sci. (including Subser. Lect. Notes Artif. Intell. Lect. Notes Bioinformatics), vol. 5304 LNCS, 2008, p. 83–97. doi:10.1007/978-3-540-88690-7-7.

[26] Nonnenmacher L, Coimbra CFM. Streamline-based method for intra-day solar forecasting through remote sensing. Sol Energy 2014;108:447–59. doi:10.1016/j.solener.2014.07.026.

[27] Dev S, Savoy FM, Lee YH, Winkler S. Short-term prediction of localized cloud motion using ground-based sky imagers. 2016 IEEE Reg. 10 Conf., IEEE; 2016, p. 2563–6. doi:10.1109/TENCON.2016.7848499.

[28] Chow CW, Belongie S, Kleissl J. Cloud motion and stability estimation for intra-hour solar forecasting. Sol Energy 2015;115:645–55. doi:10.1016/j.solener.2015.03.030.

[29] Andreas Schroeder, Christian E. Willert. Particle Image Velocimetry. vol. 112. Berlin, Heidelberg: Springer Berlin Heidelberg; 2008. doi:10.1007/978-3-540-73528-1.

[30] Chu Y, Pedro HTC, Li M, Coimbra CFM. Real-time forecasting of solar irradiance ramps with smart image processing. Sol Energy 2015;114. doi:10.1016/j.solener.2015.01.024.

[31] Li M, Chu Y, Pedro HTC, Coimbra CFM. Quantitative evaluation of the impact of cloud transmittance and cloud velocity on the accuracy of short-term DNI forecasts. Renew Energy 2016;86:1362–71. doi:10.1016/j.renene.2015.09.058.

[32] Zaher A, Thil S, Nou J. Comparative study of algorithms for cloud motion estimation using sky-imaging data. IFAC-PapersOnLine 2017;50:6108–13. doi:10.1016/j.ifacol.2017.08.1488.

[33] Reddy BS, Chatterji BN. An FFT-based technique for translation, rotation, and scale-invariant image registration. IEEE Trans Image Process 1996;5:1266–71. doi:10.1109/83.506761.

[34] Tomar G, Singh SC, Montagner JP. Sub-sample time shift and horizontal displacement measurements using phase-correlation method in time-lapse seismic. Geophys Prospect 2017;65:407–25. doi:10.1111/1365-2478.12422.

[35] Arking A, Lo RC, Rosenfeld A, Arking A, Lo RC, Rosenfeld A. A Fourier Approach to Cloud Motion Estimation. J Appl Meteorol 1978;17:735–44. doi:10.1175/1520-0450(1978)017<0735:AFATCM>2.0.CO;2.

[36] Zhenhui W, Jun Z. A PRELIMINARY STUDY OF FOURIER SERIES ANALYSIS ON CLOUD TRACKING WITH GOES HIGH TEMPORAL RESOLUTION IMAGES. J Meteorol Res 2000;14:82–94.

[37] Jun L, Fengxian Z. Cloud motion estimation from VIS and IR data of geosynchronous satellite using fourier technique. Adv Sp Res 1992;12:123–6. doi:10.1016/0273-1177(92)90206-D.

[38] Balci M, Foroosh H. Subpixel estimation of shifts directly in the Fourier domain. IEEE Trans Image Process 2006;15:1965–72. doi:10.1109/TIP.2006.873457.

[39] DeFlores LP, Nicodemus RA, Tokmakoff A. Two-dimensional Fourier transform spectroscopy in the pump-probe geometry. Opt Lett 2007;32:2966. doi:10.1364/OL.32.002966.

[40] Brackx F, De Schepper N, Sommen F. The two-dimensional Clifford-Fourier transform. J Math Imaging Vis 2006;26:5–18. doi:10.1007/s10851-006-3605-y.

[41] Bailey DH, Swarztrauber PN. A fast method for the numerical evaluation of continuous Fourier and Laplace transforms. SIAM J Sci Comput 1994;15:1105–10. doi:10.1137/0915067.

[42] Rafael Gonzalez C, Woods R. Digital Image Processing, Third Edition. Pearson Education; 2017.

[43] Ni X (Sherry), Huo X. Statistical interpretation of the importance of phase information in signal and image reconstruction. Stat Probab Lett 2007;77:447–54. doi:10.1016/j.spl.2006.08.025.

[44] Oppenheim A V., Lim JS. The Importance of Phase in Signals. Proc IEEE 1981;69:529–41. doi:10.1109/PROC.1981.12022.

[45] Mori N, Chang K A. Introduction to MPIV n.d. http://www.oceanwave.jp/softwares/mpiv.

[46] Dollár P. Piotr’s Computer Vision Matlab Toolbox (PMT) n.d. https://github.com/pdollar/toolbox.